iScience

CellPress
OPEN ACCESS

Article

Lattice-patterned collagen fibers and their dynamics in axolotl skin regeneration

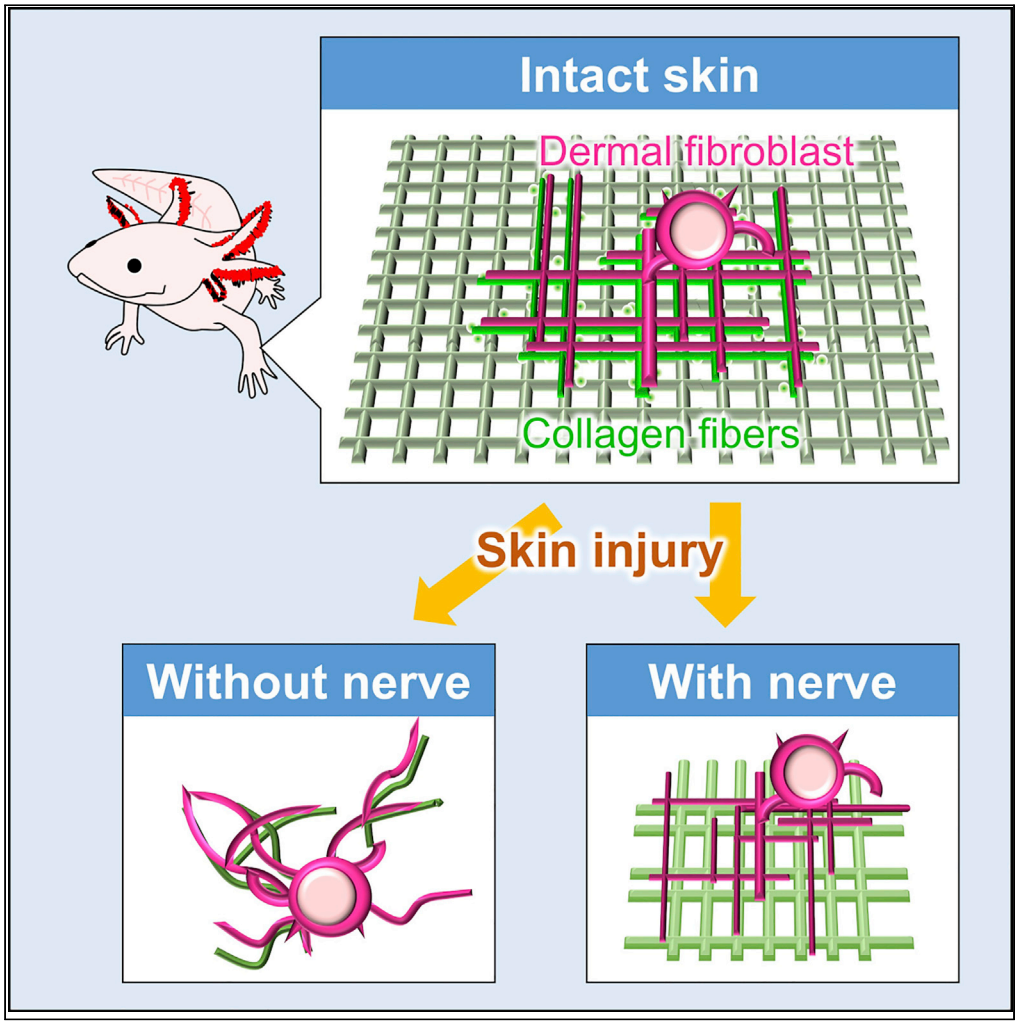

Rena Kashimoto, Saya Furukawa, Sakiya Yamamoto, ..., Tatsuya Sakamoto, Hirotaka Sakamoto, Akira Satoh

satoha@cc.okayama-u.ac.jp

Highlights

Dermal collagen synthesized by a single cell was visualized in the axolotl skin

Collagen-synthetic cells were visualized and revealed lattice-patterned filopodia

Collagen pattern was deformed after simple skin wounding

The lattice-patterned collagen was only restorable in the presence of nerves

Kashimoto et al., iScience 25, 104524
July 15, 2022
https://doi.org/10.1016/j.isci.2022.104524

iScience

CellPress
OPEN ACCESS

Article

Lattice-patterned collagen fibers and their dynamics in axolotl skin regeneration

Rena Kashimoto,[1] Saya Furukawa,[2] Sakiya Yamamoto,[2] Yasuhiro Kamei,[3] Joe Sakamoto,[3] Shigenori Nonaka,[3,4] Tomonobu M. Watanabe,[5,6] Tatsuya Sakamoto,[1,7] Hirotaka Sakamoto,[1,7] and Akira Satoh[8,9,*]

SUMMARY

The morphology of collagen-producing cells and the structure of produced collagen in the dermis have not been well-described. This lack of insights has been a serious obstacle in the evaluation of skin regeneration. We succeeded in visualizing collagen-producing cells and produced collagen using the axolotl skin, which is highly transparent. The visualized dermal collagen had a lattice-like structure. The collagen-producing fibroblasts consistently possessed the lattice-patterned filopodia along with the lattice-patterned collagen network. The dynamics of this lattice-like structure were also verified in the skin regeneration process of axolotls, and it was found that the correct lattice-like structure was not reorganized after simple skin wounding but was reorganized in the presence of nerves. These findings are not only fundamental insights in dermatology but also valuable insights into the mechanism of skin regeneration.

INTRODUCTION

The skin is the organ that covers the body. Because of its location on the surface of the body, the skin has much chance to be damaged. In the epidermis—the surface layer of the skin—keratinocytes maintain homeostasis through constant cell proliferation in the basal layer (Smart, 1970). Damage on the surface can be repaired through the constant division of keratinocytes. However, in wounds that reach the dermis in mammals, the skin is generally not regenerated (Gurtner et al., 2008). This inability to regenerate the skin can lead to a decreased quality of life (QOL) in humans. Therefore, the skin organ has been the target of extensive medical research.

Amphibians have skin structures that are comparable to those of other vertebrates. Axolotls—*Ambystoma mexicanum*—have epidermis and dermis in the skin as in mammals (Seifert et al., 2019). The epidermis consists of keratinocytes and the dermis contains collagen-synthesizing fibroblasts. Axolotl skin has no hair follicles or sweat glands, but it has glands that secrete mucus. Collagen is the major component in the axolotl dermis, as it is in mammals. Generally, collagen is the matrix that supports healthy skin and is a key determinant in the preservation of skin firmness and elasticity (Fisher et al., 2008). Type I collagen is the main type of collagen in the skin, accounting for 80%–90% of skin collagen and is produced by dermal fibroblasts (Nolte et al., 2008). The trimer of type I collagen is composed of two α1 (I) chains and one α2 (I) chain, which are produced from *Col1a1* and *Col1a2*, respectively. Synthesized procollagen is secreted via ER-to-Golgi trafficking (Jin et al., 2012; McCaughey et al., 2019). Then the N-terminal and C-terminal domains of procollagen are cleaved to form crosslinked collagen fibrils in the spaces around the fibroblast (Canty and Kadler, 2005). The collagen fibrils assemble to form collagen fibers, and the bundles of collagen fibers form the dermal collagen layers. This principle of dermal collagen has been considered to be highly conserved among vertebrates, including axolotls. Structural analysis of dermal collagen has been attempted using observation techniques such as scanning electron microscopy (SEM) (Tsuji et al., 1979), transmission electron microscopy (TEM) (Birk et al., 1991), and second-harmonic generation (SHG) imaging (Ueda et al., 2019). However, in many vertebrates, imaging of dermal collagen is difficult because of the presence of thick or haired epidermis and/or higher tissue opacity, which hinders imaging. In contrast, axolotl skin has high transparency, so much so that it is possible to observe the blood flow and bones through the skin in a small axolotl. This transparency provides advantages in the investigation using fluorescent probes in dermatological studies. Thus, axolotl skin can be used as a model for dermatological investigation.

[1]Division of Earth, Life, and Molecular Sciences, Graduate School of Natural Science and Technology, Okayama University, Okayama 700-8530, Japan

[2]Department of Biological Sciences, Faculty of Science, Okayama University, Okayama 700-8530, Japan

[3]National Institute for Basic Biology (NIBB), National Institutes for Natural Sciences, Okazaki 444-8585, Japan

[4]Exploratory Research Center for Life and Living Systems (ExCELLS), National Institutes for Natural Sciences, Okazaki 444-8585, Japan

[5]Laboratory for Comprehensive Bioimaging, RIKEN Center for Biosystems Dynamics Research (BDR), Kobe 650-0047, Japan

[6]Department of Stem Cell Biology, Research Institute for Radiation Biology and Medicine, Hiroshima University, Hiroshima 734-8553, Japan

[7]Ushimado Marine Institute (UMI), Okayama University, Setouchi 701-4303, Japan

[8]Research Core for Interdisciplinary Sciences (RCIS), Okayama University, Okayama 700-8530, Japan

[9]Lead contact

*Correspondence: satoha@cc.okayama-u.ac.jp

https://doi.org/10.1016/j.isci.2022.104524

Skin regeneration is currently one of the most important themes in dermatology. Skin wounding in mammals results in different degrees of healing depending on the depth of damage (Dunkin et al., 2007). In general, deep wounding results in scarring. Scar formation is characterized by oversynthesis and disordered orientation of collagen fibers (Gauglitz et al., 2011; Xue and Jackson, 2015). Hypersynthesis and disorganized fiber formation results in keloid scar formation. The mechanism that induces collagen abnormality has been the subject of medical investigation but has not yet been determined. In amphibians, the surrounding epidermis covers the wound surface after skin wounding (Satoh et al., 2008; Tanner et al., 2009; Yokoyama et al., 2011). Despite the depletion of full-thickness skin, the epidermis covers the wound surface within a day, and new collagen production occurs beneath the overlying epithelium (Satoh et al., 2008; Yang et al., 1999). Transiently, abnormal collagen fibers can be observed, but eventually, the histology of the wounded site becomes similar to that of normal skin (Abe et al., 2020; Seifert et al., 2012; Yokoyama et al., 2018). Keloid or scar formation has not been reported so far. Based on these observations, amphibian skin regeneration is considered to undergo epimorphic regeneration (Lévesque et al., 2010). However, because of the underdevelopment of molecular biological methods for use in amphibians, the rearrangement and recomposition of collagen fibers in skin regeneration have not been properly verified. To clarify the mechanism of skin regeneration, the dynamics of collagen fibers need to be examined in more detail. The dermatology of axolotls has great potential to advance the field because of its transparency and regenerative properties.

In the present study, we developed a method to visualize skin collagen at the single-cell level using a plasmid vector expressing fluorescent protein fusion collagen. This visualization of the collagen fibers revealed a lattice-patterned dermal collagen network, and cell morphology was simultaneously acquired. The collagen-synthesizing fibroblasts exhibited the characteristic lattice shape. We also observed the SHG signals to investigate the entire structure of axolotl dermal collagen. Based on these observations, we quantitatively analyzed axolotl skin wound healing, focusing on the collagen network. In these analyses, we found that nerve presence contributes to the reformation of the lattice-patterned dermis after skin wounding. Our findings provide new insights for dermatological biology and studies in skin wound healing.

RESULTS

The detailed structure of dermal ECM in the axolotl skin

We first confirmed the histology of the axolotl limb skin. As previously reported (Seifert et al., 2012), Picrosirius red (PSR) staining successfully visualized the axolotl dermal collagen of the axolotl lower limb (Figures 1A and 1B). The red staining could be observed between the epidermis and the muscles (Figure 1A). The dermis in the dorsal region is divided into two layers: the stratum spongiosum (SS) and the stratum compactum (SC). The SC contains dense collagen and is always observable in the lower layer of the dermis. To distinguish type I and III collagen in the SS and SC, the PSR-stained sections were observed under polarized light; type I and III collagen are shown in red and green, respectively (Figure 1B). It is evident that type I collagen is the major component of axolotl dermis. The SS consists of relatively much type III collagen than the SC. To visualize the overall structure of the dermal extracellular matrix (ECM), the decellularized dermis was prepared and observed (Figure 1C). The dermis was dissected and decellularized as previously described (Phan et al., 2015). Then, the dermal structure was observed from the inner side. The observed dermal ECM has a "lattice" pattern (Figure 1C). We also observed the entire stack of the collagen layer using SHG imaging (Figure 1D and Video S1), which can visualize the non-centrosymmetric triple-helix structure of collagen using two-photon microscopy. It was revealed that collagen fibers were oriented in a wavy string-like structure in the SS and in a lattice pattern in the SC. It is of note that such lattice patterns were not observed in the dermis of rat, *Rattus norvegicus* (Figure S1 and Video S2). Rat dermal collagen had wavy string-like fibers. Dermal ECM exhibiting a lattice pattern was reported in zebrafish, *Danio rerio* (Morris et al., 2018). Thus, the lattice structure of the dermal collagen might be unique to aquatic animals. To describe the finer structure of dermal ECM, we used SEM imaging on the decellularized dermis (Figures 1E and 1F) and observed the knitted orthogonal bundles (Figure 1F). The bundles running on the x axis and the ones on the y axis appear to take different levels at the z axis. The more focused image showed that each fiber is conjunct with thin fibers (Figures 1E and 1F). These images successfully clarified the well-oriented axolotl dermal ECM with the lattice pattern.

Observation of type I collagen structure at the single-cell level

To focus more on the detailed structure, we visualized the fibers of type I collagen in axolotl dermis by expressing fluorescent protein fusion collagen. Collagen visualization using fluorescent molecular fusion

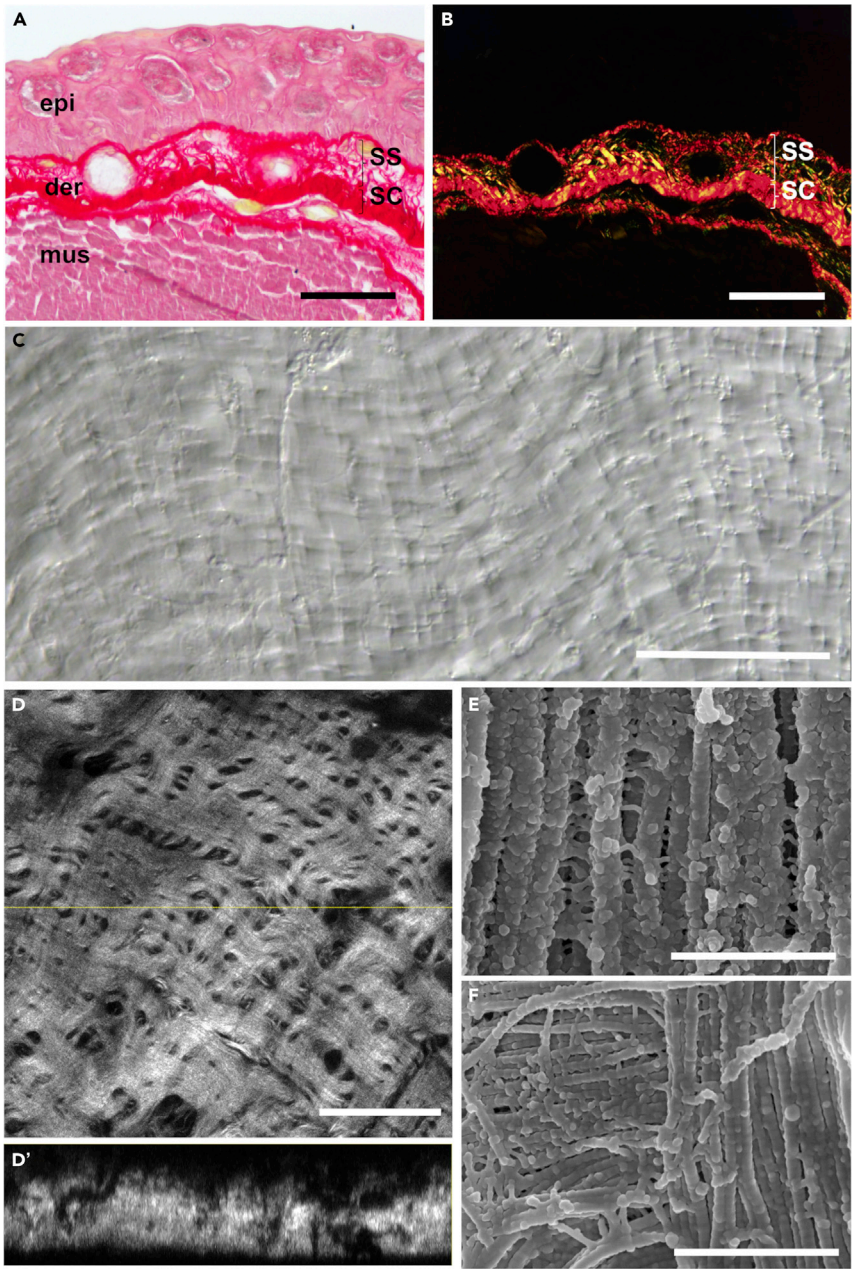

Figure 1. Axolotl dermis contains a high density of collagen fibers

(A and B) Histology of uninjured skin on axolotl limb. Tissue sample stained with Picrosirius red and photographed under unpolarized light (A) or polarized light (B). Type I collagen (red in B) is abundant in dermis. epi, epidermis; der, dermis; mus, muscle; SS, stratum spongiosum; SC, stratum compactum. Scale bars, 100 μm.

(C) Decellularized ECM of axolotl skin. Scale bar, 100 μm.

(D) SHG image (xy) of dermal collagen and its xz image (D'). Scale bar, 50 μm. See also Video S1.

(E and F) SEM imaging of decellularized dermal ECM. Bundles of collagen fibrils were aligned in parallel or orthogonal. Scale bars, 1 μm.

proteins has been performed on mice and zebrafish (Kamel-ElSayed et al., 2015; Lu et al., 2018; Morris et al., 2018). We applied the technique to axolotls. The triple-helix of type I collagen is composed of two α1 chains and one α2 chain. We constructed a plasmid vector expressing GFP-fused axolotl *Col1a2* (GFP-Col1a2) (Figure S2). After the signal sequence, GFP and *Col1a2* were connected with the GS linker. Because the N-terminal and C-terminal domains are cleaved from procollagen during collagen formation, the

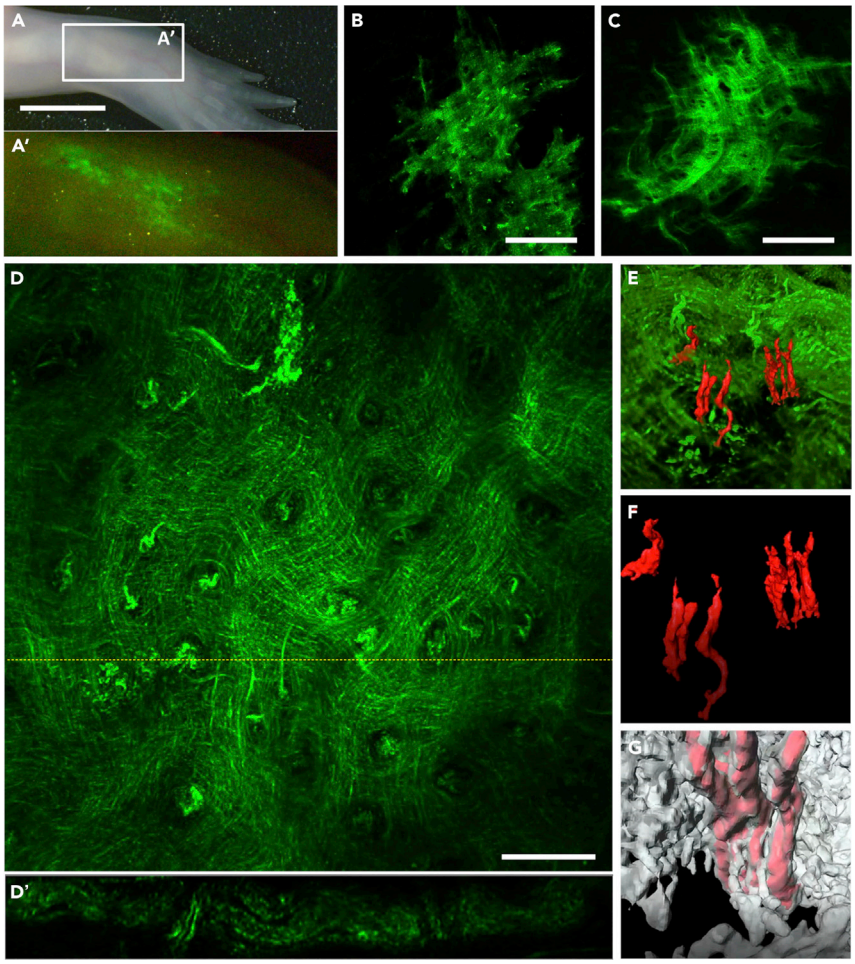

Figure 2. The lattice patterned collagen in the dermal SC

(A) *In vivo* image of GFP-collagen. Scale bar, 2 mm.

(B and C) The lattice patterned collagen mesh with pillars (B) and without pillars (C). Scale bars, 50 μm.

(D) The confocal image of the lattice patterned collagen with pillars. The images are the maximum intensity projection. Scale bar, 10 μm. (D′) The reconstituted side view of D.

(E) The confocal images were reconstituted by Amira and the selected pillars were colored in red.

(F) The pillars were extracted from the image.

(G) The lattice patterned collagen is shown in white and the pillars are in red. A few collagen fibers bridge to the pillars. See also Video S3.

N-terminal propeptide and telopeptide domain was deleted in GFP-Col1a2 (Figures S2A and S2B). The designed fusion protein is driven by a ubiquitous CMV promoter (Figure S2C). To analyze the collagen structure at the single-cell level, we chose localized transfection of the GFP-Col1a2 vector by electroporation. Plasmid vectors expressing GFP-Col1a2 were induced randomly into dermal cells, and only the GFP + collagen fibers produced by the transfected cells were labeled. We performed electroporation on the limb dermis of axolotls (n = 8). Five days after transfection, GFP signals could be detected *in vivo* (Figure 2A). The GFP signals were fiber-shaped, suggesting that the collagen fibers were visualized. To investigate further, we harvested the skin and observed it under the confocal microscope (Figures 2B–2G). The GFP signals were enhanced by immunofluorescence using anti-GFP antibodies. We successfully visualized the 100-nm-order fibril structure of type I collagen at the single-cell level. We observed the lattice-patterned GFP + collagen fibers. There were at least two patterns of lattice in the axolotl dermis. One is the lattice-patterned GFP + collagen with pillars (Figures 2B and 2D), and the other is the lattice-patterned GFP + collagen without pillars (Figure 2C). For detailed observation of the GFP + collagen fibers with pillars, the confocal images were reconstituted and analyzed (Figures 2D–2G and Video S3). The pillars were located in the hole (Figures 2D and 2D′). Usually, two to five collagen pillars were observed in a hole

(Figure 2D'). For easier understanding, we transferred the data to Amira software and segmented it by the displayed components (Figures 2E–2G and Video S3). It is apparent that there are pillars (red) in the hole and the pillars were anchored by a few fibers.

Next, we focused on the fibroblasts, which produced GFP + collagen. To visualize the morphology of fibroblasts producing type I collagen, plasmid vectors expressing mCherry at the cytoplasm were co-transfected with the GFP-Col1a2 vector. We observed the collagen-producing process by *in vivo* live imaging using the two-photon microscope (Figures 3A and 3B; n = 5). The images were taken the day after electroporation. Lattice-like fibroblasts were building collagen fibers while extending (Figure 3A) and contracting (Figure 3B) their filopodia. To analyze the structure of collagen fibers and fibroblasts with higher resolution, we observed fixed skin samples from the dermal side using a confocal microscope (Figure 3C; n = 8). Five days after electroporation, we harvested and fixed the skin. GFP signals were enhanced by immunofluorescence using the anti-GFP antibodies, and mCherry fluorescence was observed without immunostaining. The GFP + collagens had a lattice pattern (Figure 3C1). The mCherry + fibroblasts had lattice-patterned filopodia along the GFP + collagen fibers (Figure 3C2 and Video S4). The filopodia of the mCherry + cell were bifurcated at right angles at many points. The merged image reveals that the shape of the mCherry + cell and the GFP + collagen fibers overlapped (Figure 3C3). The reconstituted confocal images also revealed that the filopodia of the mCherry + cell were located by or with the GFP + collagen fibers (Figure 3C and Video S5). To confirm that the GFP + collagen fibers visualized by overexpressing GFP-Col1a2 reflected normal endogenous collagen fibers, we observed GFP + fibers overlapped with the SHG images by two-photon microscopy (Figures 4A–4C; n = 3). The orthogonal collagen bundles were visualized by SHG imaging (Figure 4A) and the GFP + collagen fibers were visualized on the identical sample (Figure 4B). The merged image shows the consistency of the fiber orientation (Figure 4C). Reconstitution of the images allowed identification of the GFP + collagens in the SC (Figure 4C'). The GFP + collagen fibers were located in the basal (inner) region of the SC, suggesting that several stacks of the lattice-patterned fibroblasts and collagen fibers form the SC. Lastly, we investigated the *Col1a1* and *Col1a2* expression of the lattice-patterned fibroblasts. In the aforementioned experiments, we electroporated the GFP-Col1a2 plasmid with the ubiquitous promoter. The promoter/enhancer enables the strong driving of a target gene regardless of cell type. To investigate whether lattice-shaped cells inherently produce type I collagen, we performed *in situ* hybridization using *Col1a1* or *Col1a2* probes with immunofluorescence of mCherry (Figures 4D and 4E; n = 4/gene). The lattice-shaped cell was identified by the mCherry signal, and the *Col1a1* and *Col1a2* expression was confirmed in the identical cells (Figures 4D and 4E). It is of note that the signal of *Col1* transcripts was always restricted in part of the fibroblasts. We also investigated whether the lattice-patterned collagen fibers forced the cells to adopt a consistent lattice shape. First, we prepared a decellularized axolotl dermal ECM as described earlier. Then, the fibroblasts collected from the dermis of a GFP transgenic axolotl were placed on the decellularized ECM. The shape of the cells was observed on day 5 of culture (Figure S3; n = 3 independent experiments). No cells adopt a lattice shape, suggesting that the lattice shape of cells is not a result of the scaffold shape. It is thus expected that dermal fibroblasts adopt a lattice-like morphology autonomously.

The structure of collagen fibers in wounded axolotl skin and regenerated axolotl limb

It is considered that the skin can be regenerated in amphibians. As mentioned before, histological observations support the idea that the amphibian skin can regenerate (Seifert et al., 2012; Yokoyama et al., 2018). However, a detailed observation focusing on collagen fibers has not yet been achieved. Therefore, we focused on the collagen fibers in axolotl wounded skin (Figure 5). The full thickness of the skin was removed, and the wounded portion could be identified at 20 and 50 days post-injury (dpi) (Figure 5A). PSR staining revealed that the collagen layer of the dermis could be restored after the skin removal (Figure 5B; n = 3/time point). Dermal gland formation could be observed at 20 dpi and SC formation was evident at 50 dpi. These findings are quite consistent with those of previous research (Seifert et al., 2012). To reveal the collagen structures, we observed the overall collagen structure by SHG imaging (Figure 5C; n = 6). The collagen structures were not orientated like those in the normal skin (Figures 5C vs 1D). No lattice-patterned collagen bundles were observed in the SHG imaging (Figure 5C). To investigate this further, we electroporated the GFP-Col1a2 vector to the wounded skin (45 dpi), and the sample was then fixed 5 days after the electroporation (50 dpi) (n = 6). The collagen structure was not lattice-patterned but was instead shrunken and disorganized (Figure 5D). The fibroblasts did not consistently adopt a lattice shape (Figure 5E). The merged image shows that the fibroblasts with disorganized filopodia synthesized disorganized collagen fibers (Figure 5F). This is consistent with the results of SHG imaging. The

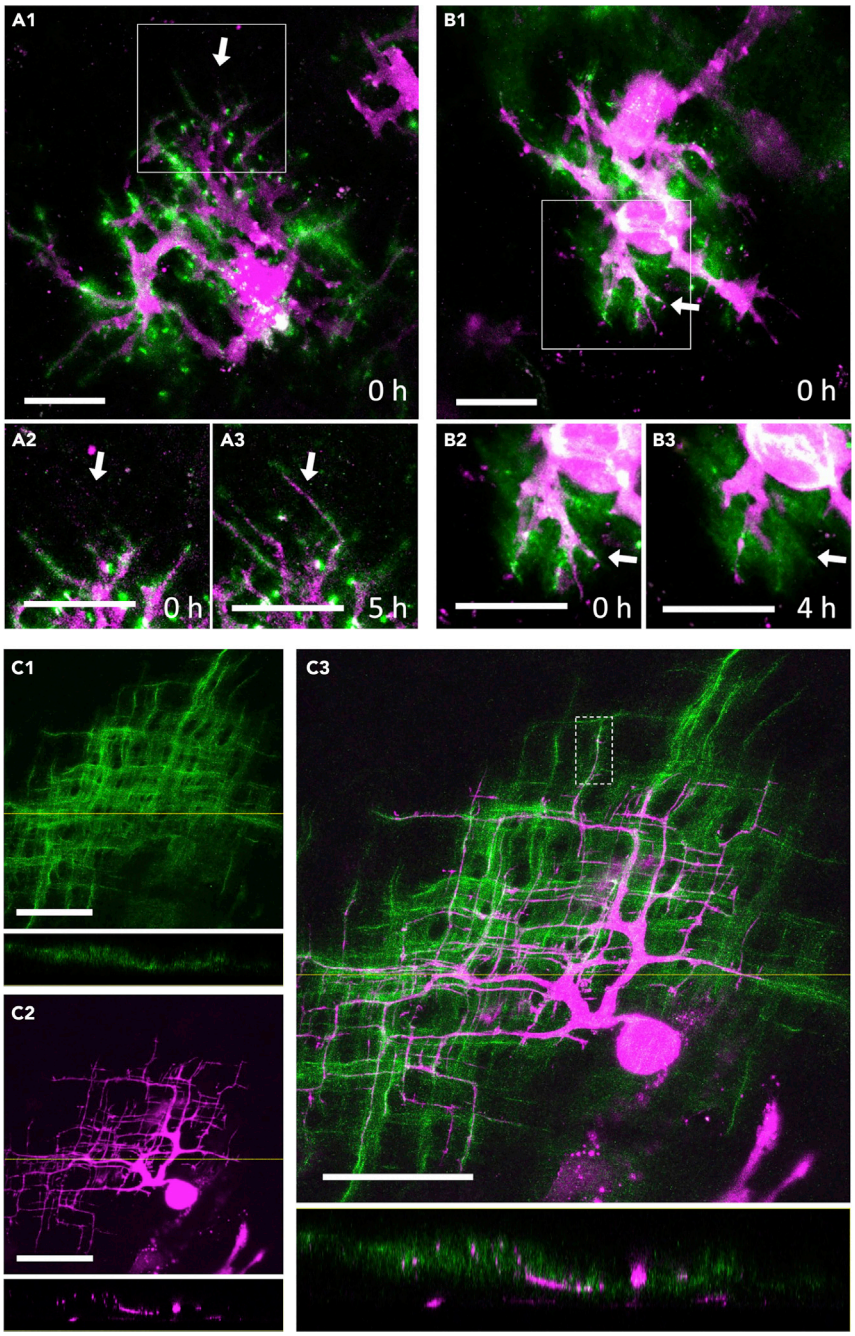

Figure 3. The lattice patterned collagen fibers and collagen-producing cells

(A and B) *In vivo* time-lapse images of collagen-producing fibroblasts with their filopodia extending (A) and contracting (B). Green indicates the produced GFP-labeled type I collagen. Magenta indicates the mCherry expressed at the cytoplasm. Scale bars in A-B, 25 μm.

(C) Confocal images of a fixed skin sample. A piece of skin was fixed 5 days after transfection and photographed from the dermal side. GFP-labeled collagen fibers (green) were constructed around the lattice-like filopodia (magenta). Lower panels are the reconstituted side view of the lined position in upper panels. Scale bars in C, 50 μm. The images are the maximum intensity projection. The morphology of the lattice-patterned fibroblast was analyzed three-dimensionally (Video S4). From the data of confocal images within the white dotted line in C3, three-dimensional analysis movie of mCherry + filopodia and GFP + collagen was created (Video S5).

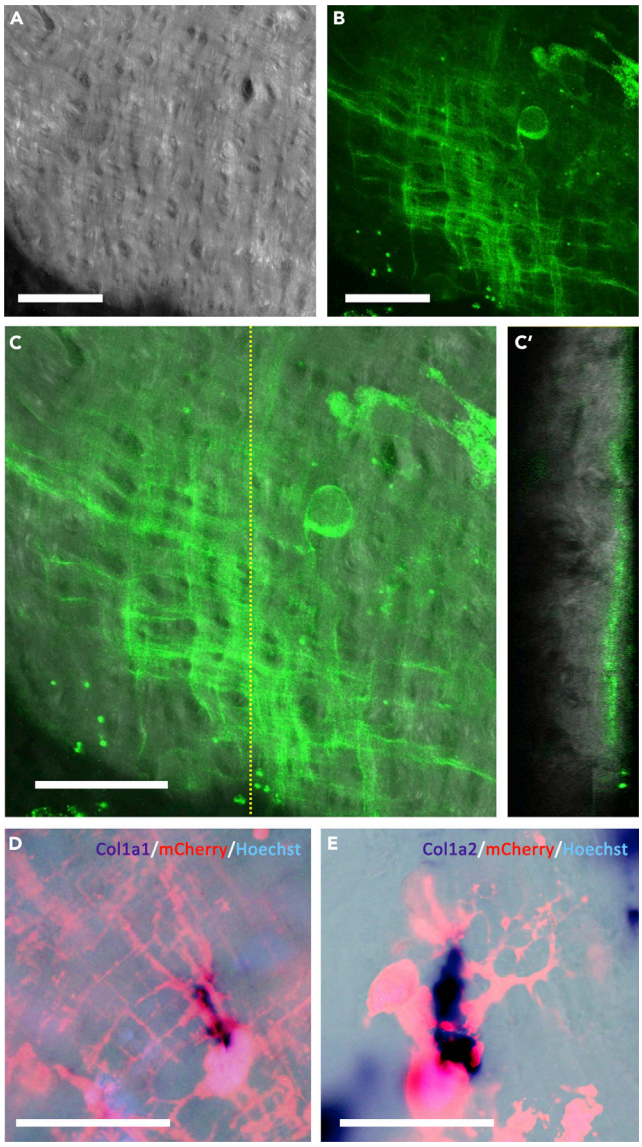

Figure 4. The relationship between the GFP-Col1a2 and the native fibers of type I collagen

(A) SHG image of the maximum intensity projection.

(B) GFP-Col1a2.

(C) The merged image. (C′) the side view of the reconstituted image at the position indicated by the line in C.

(D and E) The images of the section that received the immunofluorescence for mCherry and *in situ* hybridization for *Col1a1* (D) and *Col1a2* (E). Nuclei were visualized by Hoechst. The merged images were shown. Scale bars, 50 μm.

disorganization of the collagen fibers was even observable in the wounded skin at 120 dpi (Figure S4; n = 3), suggesting that axolotl skin regeneration is not epimorphic in terms of collagen orientation.

Axolotls are well recognized for having organ-level regeneration, including limb regeneration. We were interested in the dermis structures in a regenerated limb after limb amputation. To investigate this, we amputated axolotl limbs and observed the dermis in the fully regenerated limb at 50 days postamputation (dpa) (Figure 6A). PSR staining revealed that the ECM deposition was poor in the dermis at 20 dpa and organized at 50 dpa (Figure 6B; n = 3/time point). The SHG imaging clarified that the lattice-patterned collagen bundles were restored at 50 dpa (Figure 6C; n = 5). The collagen synthesis at the single-cell level was visualized by the electroporation of GFP-Col1a2 vectors. The electroporation was performed at 45 dpa and the sample was fixed at 50 dpa (n = 7). Consistently, GFP + collagen fibers with the lattice pattern could

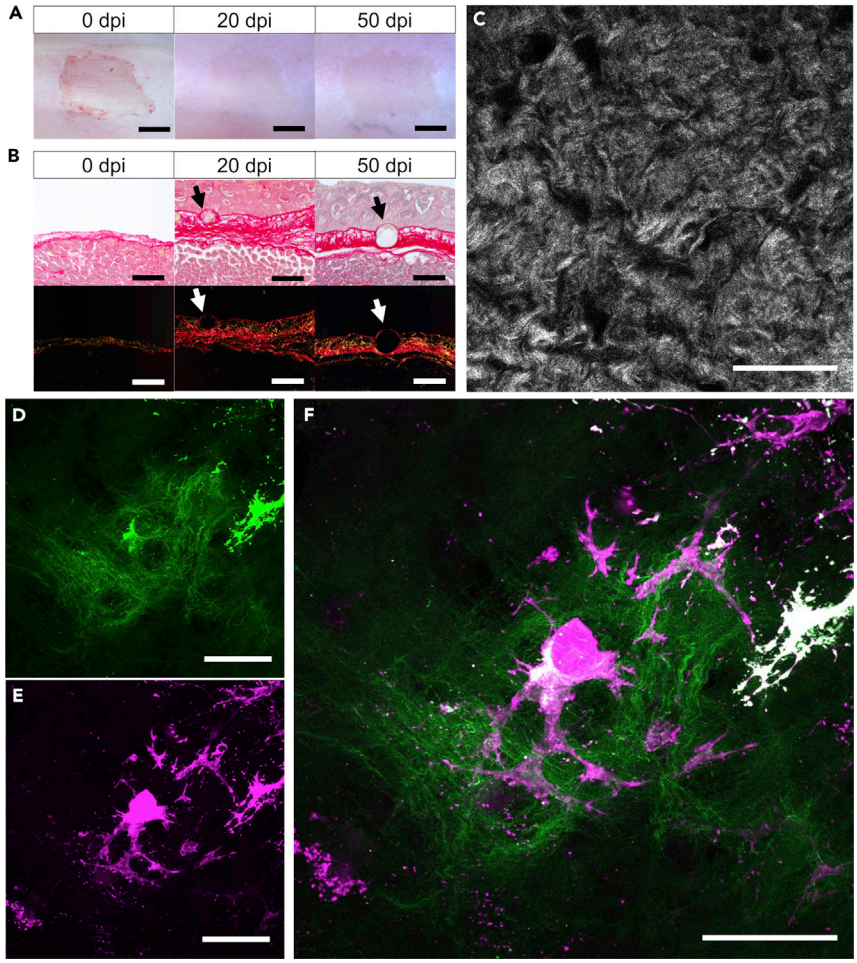

Figure 5. Collagen fibers in axolotl wounded skin

(A) Time course of axolotl skin wound healing. dpi, day post-injury. Scale bars, 1 mm.

(B) PSR staining of the wounded axolotl skin. Arrows indicate the regenerated dermal glands. Scale bars in A and B, 100 μm.

(C) Representative single z section in the stack of SHG images.

(D–F) GFP-Col1a2 and mCherry (cytoplasm) signal in the wounded skin at 50 days post-injury. The images were reconstituted from the confocal images with maximum intensity projection. (D) GFP-Col1a2. (E) mCherry. (F) The merged image. Scale bars in C-F, 50 μm.

be observed in the dermis of the regenerated limb (Figure 6D). The GFP + collagen synthesizing fibroblasts also adopted the lattice shape (Figure 6E). The merged image reveals that the lattice-shaped cells were restored and can synthesize the lattice-patterned collagen fibers (Figure 6F). These results indicate that the dermis is fully regenerated in a regenerated limb after limb amputation.

To quantify the collagen orientation in axolotl dermis, we performed a Fourier transformation-based assay (Figures 7 and S5; n = 3/condition). The SHG imaging provides the whole-scale fiber orientation at the fiber level. Thus, we considered that the fiber orientation could be quantified from SHG images. For this purpose, we applied Fourier transformation to the SHG images (Figures 7F–7M and S5). As mentioned before, the orientation of collagen fibers is different between the SS and the SC in the dermis, and only collagen in the SC adopts a lattice pattern (Figures 1A, 1B, 1D′ and Video S1). To evaluate the orientation of the dense collagen fibers in the SC, five sequential SHG images showing a typical fiber phenotype were selected from the stack of SHG images for each sample (Figures 7F–7I). Then, the selected images were Fourier transformed and subsequently analyzed statistically (Figures 7J–7M and S5). In the intact dermis, two peaks can be observed (Figures 7J and S5A), suggesting that fiber flow exhibits two-way directionality. In the dermis in the wounded skin, we observed one-way directionality as the single peak (Figures 7M and S5D).

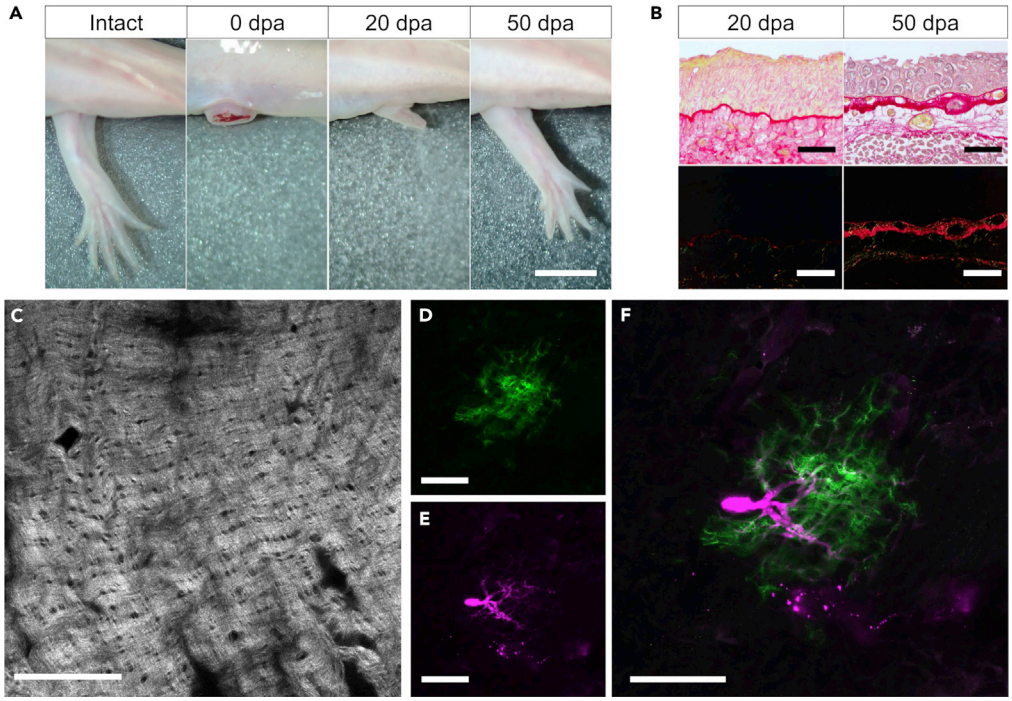

Figure 6. Collagen fibers in the axolotl amputated limbs

(A) The time course of axolotl limb regeneration. dpa, day postamputation. Scale bar, 1 cm.

(B) PSR staining in the regenerated limb. The right and the left column show the 20 dpa and 50 dpa sample, respectively. The top panels are the images taken under the unpolarized light, and the bottom panels are the images taken under the polarized light. Scale bars, 100 μm.

(C) Representative single z section in the stack of SHG images (50 dpa).

(D–F) GFP-Col1a2 and mCherry (cytoplasm) signal in the regenerated limb skin (50 dpa). The images were reconstituted from the confocal images with maximum intensity projection. Scale bars in C-F, 50 μm.

Regarding the dermis in the regenerated limb, the directionality of the fibers could be observed as two peaks (Figures 7K and S5B). We also investigated the nerve-deviated wounded skin (Figures 7D, 7H, 7L, and S5C). According to previous studies, the nerve deviation to the wounded skin can induce an ectopic blastema, suggesting the initiation of the limb regeneration process (Endo et al., 2004; Makanae and Satoh, 2012). However, the induced ectopic blastema regresses without forming any structure in most cases and flattened healed skin is formed in the end (Endo et al., 2004). Here, we investigated the dermis collagen after the disappearance of ectopic blastema formation. The nerve-deviated wounded skin showed a similar pattern of collagen fibers to that in the regenerated limb (Figures 7D and S5C). Consistently, the Fourier transformation analysis data revealed two weak peaks (Figures 7L and S5C). These results suggest that nerve presence improves in dermal collagen fiber reformation with two-way directionality.

DISCUSSION

Macroscale observation of axolotl dermal collagen

To date, the structure of axolotl skin has been determined by histological observations. Recently, detailed histology of axolotl skin and its regeneration process was reported (Seifert et al., 2012). In this research, the collagen layer of the dermis was used as an indicator of skin regeneration; few studies focused on the structure of collagen fibers. In this study, we reexamined the dermal collagen layer to evaluate skin regeneration in axolotls and found that the collagen fibers had a marked geometric lattice structure in the dermal SC (Figures 1C and 1D). It has not been previously clarified that the dense collagen layer of the SC is composed of collagen fiber bundles that are orthogonal in the two-dimensional direction. PSR staining revealed that the collagen layer is composed mainly of type I collagen with some type III collagen (Figures 1A and 1B). SEM analysis suggests that the individual collagen fibrils are bound together by fine microfibrils (Figures 1E and 1F). It remains unknown, however, how collagen bundles are formed in axolotl dermis. More detailed analysis to reveal the specific molecules that bind these collagen fibers is needed. At the fiber level, the

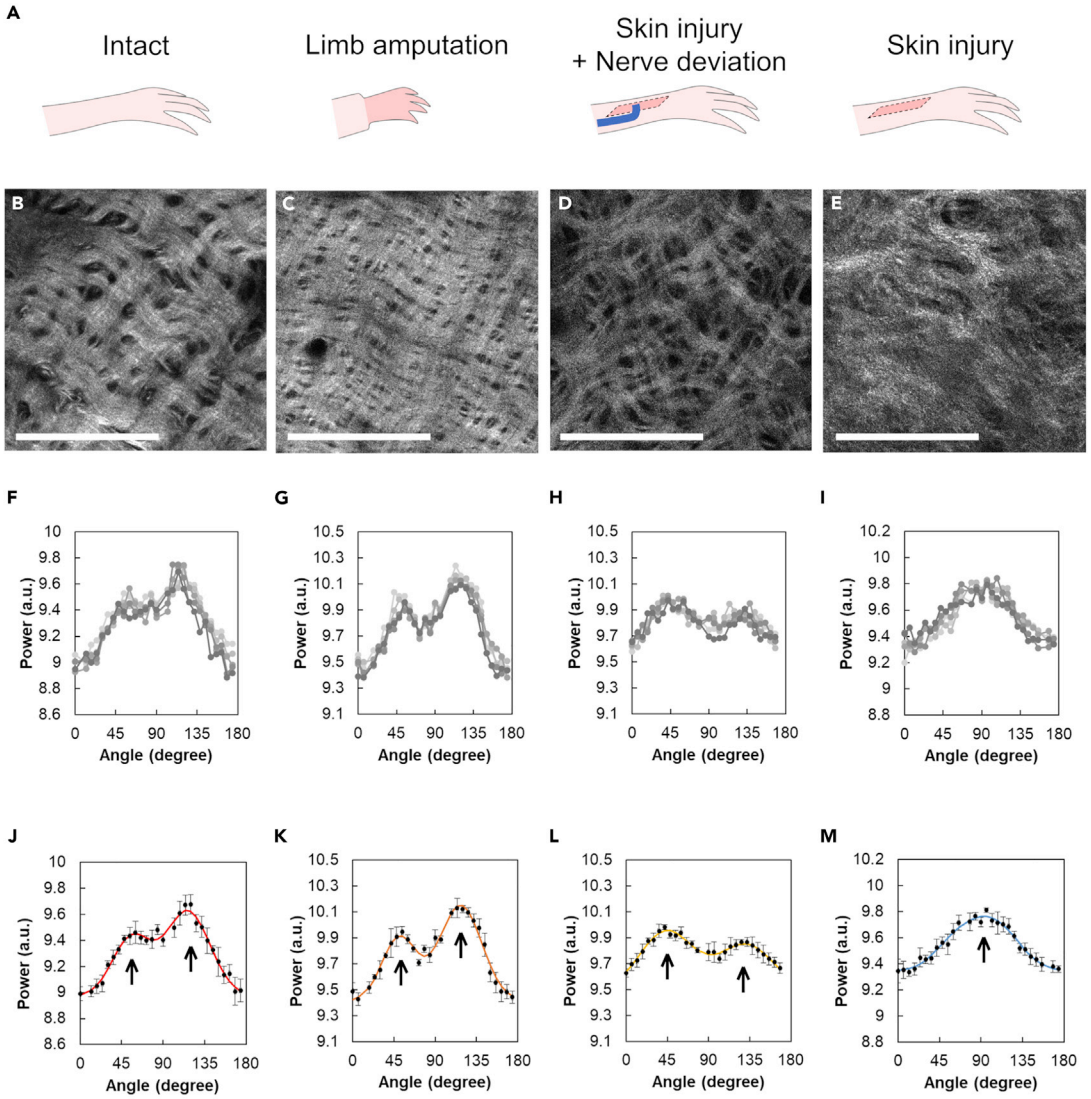

Figure 7. Quantification of the orientation of collagen fibers in SC by the Fourier transformation-based assay of SHG images

Collagen orientation of intact skin (B, F, J), skin on the regenerated limb at 50 dpa (C, G, K), injured skin with nerve deviation at 50 dpi (D, H, L), and injured skin at 50 dpi (E, I, M) were compared. dpi, day post-injury; dpa, day postamputation.

(A) Schematic showing the condition of each skin sample.

(B–E) Representative SHG images for each condition. Scale bars in B-E, 50 μm.

(F–I) The intensity of each angle of Fourier transformed SHG images. Each of five lines indicates a slice of SHG image.

(J–M) The average intensity ±SD of five selected slices of SHG images and approximate curves by Gaussian fitting. The arrows indicate the position of the peaks. The graphs of intact skin (J, red), regenerated limb skin (K, orange), and injured skin with nerve deviation (L, yellow) had two peaks, whereas the graph of injured skin without nerve deviation (M, blue) had one peak. See also Figure S5 and Table S1.

SHG imaging indicates that the lattice of collagen bundles is a structure created by the aggregation of many collagen fibers. However, how the fiber organization corresponds to the warp and weft remains unknown. The transparent skin of axolotls contributes to revealing the well-organized lattice structure and aids further studies in dermatology.

Single-cell scale observation of axolotl dermal collagen

In this study, we succeeded in visualizing the structure of dermal collagen at the single-cell level. To visualize collagen, we used a plasmid vector carrying the GFP-collagen fusion protein (Figure S2). The design of the vector was based on the previously reported papers in *D. rerio* (Morris et al., 2018). In

addition, the electroporation method we used in the present study enabled visualization at the single-cell level (Figures 2 and 3). In this study, we used plasmid vectors driven by ubiquitous CMV promoters, so all transfected cells were expected to express GFP-Col1a2 protein intracellularly regardless of cell type. For proper secretion of type I collagen, two Col1a1 and one Col1a2 should form triple-helical structure before secretion. If the triple-helical structure is not suitably formed, the secretion is inhibited (Birk et al., 1991; Canty and Kadler, 2005; Na, 1989). Therefore, it is likely that the innate dermal type I collagen is visualized by our method using GFP-Col1a2 plasmid. We found that there are at least two patterns of collagen woven by a single axolotl dermal fibroblast (Figures 2B and 2C). We observed one with a simple lattice and the other with pillar structures (Figures 2B and 2C). The role of each structure is not yet known, but the existence or the absence of the collagen pillars suggests some differences in physical properties. Visualization of a cell body showed the spatial relationship between the collagen fibers and the cells. Surprisingly, the cell body itself was found to have a lattice-like structure. To the best of our knowledge, this lattice-like cell morphology has not yet been reported in fibroblasts. It remains unclear whether cell morphology and fiber organization are axolotl specific. The formation mechanism of the lattice-patterned collagen structure also remains unknown. This orthogonal morphology of fibroblasts may be a passive result of the scaffold structure. However, no such cell extension was observed when dermal fibroblasts were cultured on the decellularized axolotl dermal collagen (Figure S3). The result, therefore, suggests that the orthogonal cell morphology might be spontaneous. More detailed time-lapse observation will help reveal the mechanism by which fibroblasts adopt orthogonal morphology and synthesize collagen fibers.

Collagen reconstitution in wound healing and regeneration

Skin regeneration is currently one of the most important research targets in dermatology and plastic surgery. It is considered that axolotls can regenerate their skin. Although this skin regeneration is epimorphic in the histological view, our results suggest that axolotl skin regeneration is hypomorphic when the collagen structure is evaluated at the fiber level. The fiber orientation of collagen is important for determining the elasticity and stiffness of the skin. If the orderliness of collagen fiber orientation supports the stiffness and elasticity of the skin, then disorganized fiber orientation would lead to disorganized skin functionality. From this point of view, the wound-healed skin of axolotls may be physiologically functional but incomplete in terms of physical function. The development of a biological technique to measure the physical properties of the skin is necessary to clarify this issue. In the present study, we also revealed that the structure of the collagen fibers was restored in the skin of a regenerated limb (Figures 6 and 7). In limb regeneration, the developmental program of the limb is considered to be reactivated (Gerber et al., 2018; Muneoka and Bryant, 1982; Satoh et al., 2015). Thus, it is highly likely that the developmental process is also recapitulated in skin construction as part of limb regeneration, and this may provide great insight into skin regeneration. If the developmental program is able to correctly orient the collagen fibers, then this could be a perfect solution for regenerating functional skin. Seifert et al. have performed research on the reactivation mechanism of developmental genes, which promote skin regeneration (Seifert et al., 2019). The remaining questions are whether the developmental program is activated in the event of skin damage and what the specific gene flow of the skin developmental program is. The search for factors that can restart the developmental program will be a major target in the quest for complete skin regeneration.

In the present study, we also demonstrated that nerve deviation improves the collagen reconstitution in skin wound healing (Figures 7 and S5). In the presence of nerves, the lattice pattern of the collagen network was recovered well compared to that without nerves. It is well-known that nerve presence triggers limb regeneration responses in axolotl limb regeneration (Satoh et al., 2015). As mentioned earlier, limb regeneration needs to reactivate developmental genes. From this point of view, nerve presence might reactivate the skin developmental program at the wounded site. As in the amputated limb, reactivation of the developmental program might lead to regeneration of the dermal collagen network. It remains unknown if the same nerve factors that can trigger limb regeneration processes play a role in the reconstitution of the dermal collagen network. Future research is needed to identify the nerve-derived molecules that can induce the complete pattern of the dermal collagen network.

Limitations of the study

To visualize dermal type I collagen and collagen-producing fibroblasts at the single-cell level, we used an electroporation method with plasmid vectors driven by ubiquitous promoters. This inevitably causes some damage to the skin tissues. The potential damage to the skin by the electroporation might cause some deformity of

collagen fibers. The other potential technical limitation in this study is the lack of high-resolution, long-term data capturing the collagen vesicles secreted by the cells. It will be a future challenge to elucidate how hierarchical collagen fibers are woven together by the lattice-patterned cells. To overcome this challenge, it is necessary to establish long-term culture conditions optimized for axolotl cells and to develop fluorescent proteins that are resistant to photobleaching. In our preliminary challenge, it was impossible to keep axolotl cells/tissues healthy for sufficient time to monitor the process *in vitro*. Besides, repeated laser exposure caused severe photobleaching, making the continuous capture of images difficult.

STAR★METHODS

Detailed methods are provided in the online version of this paper and include the following:

- KEY RESOURCES TABLE
- RESOURCE AVAILABILITY
  - Lead contact
  - Materials availability
  - Data and code availability
- EXPERIMENTAL MODEL AND SUBJECT DETAILS
- METHOD DETAILS
  - Skin wounding and limb amputation
  - Histology
  - Plasmid transfection
  - *In vivo* live imaging of collagen-producing process
  - Immunofluorescence
  - *In situ* hybridization
  - SEM and SHG imaging
  - Decellularization of the dermis and cell culture
- QUANTIFICATION AND STATISTICAL ANALYSIS
  - Analysis for the orientation of collagen fibers

SUPPLEMENTAL INFORMATION

Supplemental information can be found online at https://doi.org/10.1016/j.isci.2022.104524.

ACKNOWLEDGMENTS

We are grateful to R. Iwata and T. Satoh for their laboratory work. We thank Dr. Kaneshiro for his critical discussion and some trial experiments. We received intangible support from Olympus in our early works on collagen imaging, for which we are grateful to Mr. Takeshita (Okuma/Olympus). We also thank Dr. S. Aizawa for rat skin preparation. We thank the NIBB Bioimage Analysis Training Course 2021 (sponsored by ABiS: JSPS KAKENHI Grant Number JP16H06280) for teaching basic knowledge of image analysis. Axolotls were obtained through Hiroshima University Amphibian Research Funding. This work is supported by a JSPS KAKENHI grant-in-aid for scientific research (B) (#20H03264 to AS), JST SPRING (#JPMJSP2126 to RK), Koyanagi Foundation (to AS), and NIBB Collaborative Research Program for integrative imaging (20-514 and 21-411 to YK and AS).

AUTHOR CONTRIBUTIONS

Investigation, Data Collection, Data Analysis, and Writing – Original Draft, R.K.; Supportive Investigation and Animal Housing, S.Y. and S.F.; Confocal Imaging and SHG Imaging, Y.K., S.N., J.S., and H.S.; Fourier Transformation and Statistical Analysis, T.W.; Investigation, Experimental Design, Conceptualization, Supervision, Writing–Review and editing, Project Administration, and Funding Acquisition, A.S.

DECLARATION OF INTERESTS

The authors declare no competing interests.

Received: January 31, 2022
Revised: May 2, 2022
Accepted: May 30, 2022
Published: July 15, 2022

REFERENCES

Abe, G., Hayashi, T., Yoshida, K., Yoshida, T., Kudoh, H., Sakamoto, J., Konishi, A., Kamei, Y., Takeuchi, T., Tamura, K., and Yokoyama, H. (2020). Insights regarding skin regeneration in non-amniote vertebrates: skin regeneration without scar formation and potential step-up to a higher level of regeneration. Semin. Cell Dev. Biol. *100*, 109–121. https://doi.org/10.1016/j.semcdb.2019.11.014.

Birk, D.E., Silver, F.H., and Trelstad, R.L. (1991). Matrix assembly. In Cell Biology of Extracellular Matrix, Second Edition, E.D. Hay, ed. (Springer), pp. 221–254.

Canty, E.G., and Kadler, K.E. (2005). Procollagen trafficking, processing and fibrillogenesis. J. Cell Sci. *118*, 1341–1353. https://doi.org/10.1242/jcs.01731.

Dunkin, C.S.J., Pleat, J.M., Gillespie, P.H., Tyler, M.P.H., Roberts, A.H.N., and McGrouther, D.A. (2007). Scarring occurs at a critical depth of skin injury: precise measurement in a graduated dermal scratch in human volunteers. Plast. Reconstr. Surg. *119*, 1722–1732. https://doi.org/10.1097/01.prs.0000258829.07399.f0.

Endo, T., Bryant, S.V., and Gardiner, D.M. (2004). A stepwise model system for limb regeneration. Dev. Biol. *270*, 135–145. https://doi.org/10.1016/j.ydbio.2004.02.016.

Fisher, G.J., Varani, J., and Voorhees, J.J. (2008). Looking older: fibroblast collapse and therapeutic implications. Arch. Dermatol. *144*, 666–672. https://doi.org/10.1001/archderm.144.5.666.

Gauglitz, G.G., Korting, H.C., Pavicic, T., Ruzicka, T., and Jeschke, M.G. (2011). Hypertrophic scarring and keloids: pathomechanisms and current and emerging treatment strategies. Mol. Med. *17*, 113–125. https://doi.org/10.2119/molmed.2009.00153.

Gerber, T., Murawala, P., Knapp, D., Masselink, W., Schuez, M., Hermann, S., Gac-Santel, M., Nowoshilow, S., Kageyama, J., Khattak, S., et al. (2018). Single-cell analysis uncovers convergence of cell identities during axolotl limb regeneration. Science *362*, eaaq0681. https://doi.org/10.1126/science.aaq0681.

Gurtner, G.C., Werner, S., Barrandon, Y., and Longaker, M.T. (2008). Wound repair and regeneration. Nature *453*, 314–321. https://doi.org/10.1038/nature07039.

Jin, L., Pahuja, K.B., Wickliffe, K.E., Gorur, A., Baumgärtel, C., Schekman, R., and Rape, M. (2012). Ubiquitin-dependent regulation of COPII coat size and function. Nature *482*, 495–500. https://doi.org/10.1038/nature10822.

Kamel-ElSayed, S.A., Tiede-Lewis, L.M., Lu, Y., Veno, P.A., and Dallas, S.L. (2015). Novel approaches for two and three dimensional multiplexed imaging of osteocytes. Bone *76*, 129–140. https://doi.org/10.1016/j.bone.2015.02.011.

Lévesque, M., Villiard, É., and Roy, S. (2010). Skin wound healing in axolotls: a scarless process. J. Exp. Zool. B Mol. Dev. Evol. *314*, 684–697. https://doi.org/10.1002/jez.b.21371.

Lu, Y., Kamel-El Sayed, S.A., Wang, K., Tiede-Lewis, L.M., Grillo, M.A., Veno, P.A., Dusevich, V., Phillips, C.L., Bonewald, L.F., and Dallas, S.L. (2018). Live imaging of type I collagen assembly dynamics in osteoblasts stably expressing GFP and mCherry-tagged collagen constructs. J. Bone Miner. Res. *33*, 1166–1182. https://doi.org/10.1002/jbmr.3409.

Makanae, A., and Satoh, A. (2012). Early regulation of axolotl limb regeneration. Anat. Rec. *295*, 1566–1574. https://doi.org/10.1002/ar.22529.

McCaughey, J., Stevenson, N.L., Cross, S., and Stephens, D.J. (2019). ER-to-Golgi trafficking of procollagen in the absence of large carriers. J. Cell Biol. *218*, 929–948. https://doi.org/10.1083/jcb.201806035.

Mitogawa, K., Makanae, A., Satoh, A., and Satoh, A. (2015). Comparative analysis of cartilage marker gene expression patterns during axolotl and Xenopus limb regeneration. PLoS One *10*, e0133375. https://doi.org/10.1371/journal.pone.0133375.

Morris, J.L., Cross, S.J., Lu, Y., Kadler, K.E., Lu, Y., Dallas, S.L., and Martin, P. (2018). Live imaging of collagen deposition during skin development and repair in a collagen I - GFP fusion transgenic zebrafish line. Dev. Biol. *441*, 4–11. https://doi.org/10.1016/j.ydbio.2018.06.001.

Muneoka, K., and Bryant, S.V. (1982). Evidence that patterning mechanisms in developing and regenerating limbs are the same. Nature *298*, 369–371. https://doi.org/10.1038/298369a0.

Na, G.C. (1989). Monomer and oligomer of type I collagen: molecular properties and fibril assembly. Biochemistry *28*, 7161–7167. https://doi.org/10.1021/bi00444a005.

Nolte, S.V., Xu, W., Rennekampff, H.O., and Rodemann, H.P. (2008). Diversity of fibroblasts – a review on implications for skin tissue engineering. Cells Tissues Organs *187*, 165–176. https://doi.org/10.1159/000111805.

Phan, A.Q., Lee, J., Oei, M., Flath, C., Hwe, C., Mariano, R., Vu, T., Shu, C., Dinh, A., Simkin, J., et al. (2015). Positional information in axolotl and mouse limb extracellular matrix is mediated via heparan sulfate and fibroblast growth factor during limb regeneration in the axolotl (Ambystoma mexicanum). Regeneration *2*, 182–201. https://doi.org/10.1002/reg2.40.

Satoh, A., Graham, G.M.C., Bryant, S.V., and Gardiner, D.M. (2008). Neurotrophic regulation of epidermal dedifferentiation during wound healing and limb regeneration in the axolotl (Ambystoma mexicanum). Dev. Biol. *319*, 321–335. https://doi.org/10.1016/j.ydbio.2008.04.030.

Satoh, A., Mitogawa, K., and Makanae, A. (2015). Regeneration inducers in limb regeneration. Dev. Growth Differ. *57*, 421–429. https://doi.org/10.1111/dgd.12230.

Seifert, A.W., Monaghan, J.R., Voss, S.R., and Maden, M. (2012). Skin regeneration in adult axolotls: a blueprint for scar-free healing in vertebrates. PLoS One *7*, e32875. https://doi.org/10.1371/journal.pone.0032875.

Seifert, A.W., Cook, A.B., and Shaw, D. (2019). Inhibiting fibroblast aggregation in skin wounds unlocks developmental pathway to regeneration. Dev. Biol. *455*, 60–72. https://doi.org/10.1016/j.ydbio.2019.07.001.

Smart, I.H.M. (1970). Variation in the plane of cell cleavage during the process of stratification in the mouse epidermis. Br. J. Dermatol. *82*, 276–282. https://doi.org/10.1111/j.1365-2133.1970.tb12437.x.

Tanner, K., Ferris, D.R., Lanzano, L., Mandefro, B., Mantulin, W.W., Gardiner, D.M., Rugg, E.L., and Gratton, E. (2009). Coherent movement of cell layers during wound healing by image correlation spectroscopy. Biophys. J. *97*, 2098–2106. https://doi.org/10.1016/j.bpj.2009.06.052.

Tsuji, T., Lavker, R.M., and Kligman, A.M. (1979). A new method for scanning electron microscopic visualization of dermal elastic fibres. J. Microsc. *115*, 165–173. https://doi.org/10.1111/j.1365-2818.1979.tb00166.x.

Ueda, M., Saito, S., Murata, T., Hirano, T., Bise, R., Kabashima, K., and Suzuki, S. (2019). Combined multiphoton imaging and biaxial tissue extension for quantitative analysis of geometric fiber organization in human reticular dermis. Sci. Rep. *9*, 10644. https://doi.org/10.1038/s41598-019-47213-5.

Xue, M., and Jackson, C.J. (2015). Extracellular matrix reorganization during wound healing and its impact on abnormal scarring. Adv. Wound Care (New Rochelle) *4*, 119–136. https://doi.org/10.1089/wound.2013.0485.

Yang, E.V., Gardiner, D.M., Carlson, M.R.J., Nugas, C.A., and Bryant, S.V. (1999). Expression of Mmp-9 and related matrix metalloproteinase genes during axolotl limb regeneration. Dev. Dyn. *216*, 2–9. https://doi.org/10.1002/(sici)1097-0177(199909)216:1<2::aid-dvdy2>3.0.co;2-p.

Yokoyama, H., Maruoka, T., Aruga, A., Amano, T., Ohgo, S., Shiroishi, T., and Tamura, K. (2011). Prx-1 expression in Xenopus laevis scarless skin-wound healing and its resemblance to epimorphic regeneration. J. Invest. Dermatol. *131*, 2477–2485. https://doi.org/10.1038/jid.2011.223.

Yokoyama, H., Kudo, N., Todate, M., Shimada, Y., Suzuki, M., and Tamura, K. (2018). Skin regeneration of amphibians: a novel model for skin regeneration as adults. Dev. Growth Differ. *60*, 316–325. https://doi.org/10.1111/dgd.12544.

STAR★METHODS

KEY RESOURCES TABLE

REAGENT or RESOURCE	SOURCE	IDENTIFIER
Antibodies		
Rabbit polyclonal anti-GFP	MBL	Cat#598; RRID:AB_591819
Rabbit monoclonal anti-mCherry (E5D8F)	Cell Signaling Technology	Cat#43590; RRID:AB_2799246
Goat anti-rabbit, Alexa Fluor 488	Thermo Fisher Scientific	Cat#A32731; RRID:AB_2633280
Donkey anti-rabbit, Alexa Fluor 594	Thermo Fisher Scientific	Cat#A-21207; RRID:AB_141637
Sheep anti-Digoxigenin Fab fragments, AP conjugated	Roche	Cat#11093274910; RRID:AB_514497
Critical commercial assays		
Picrosirius Red Stain Kit	Polysciences	24901
Experimental models: Organisms/strains		
Ambystoma mexicanum: wildtype	Amphibian Research Center (Hiroshima University)	N/A
Ambystoma mexicanum: GFP	Ambystoma Genetic Stock Center	RRID: AGSC_110E
Rattus norvegicus: F344 Fischer	Gift from Dr. S. Aizawa	RRID:RGD_60994
Oligonucleotides		
Col1a1 RNA probe (AXOLOTL-OMICS, Am_2.2, AC_02200027944.1)	Mitogawa et al. (2015)	N/A
Col1a2 RNA probe (AXOLOTL-OMICS, Am_2.2, AC_02200044881.1)	This paper	N/A
Recombinant DNA		
pCS2-CMV-ss-AcGFP-axCol1a2	This paper	N/A
pCS2-CMV-mCherry	This paper	N/A
Software and algorithms		
Fiji	Fiji	https://imagej.net/software/fiji/
Amira Software	Thermo Fisher Scientific	http://www.fei.com/software/amira-3d-for-life-sciences/
Leica Application Suite X	Leica	https://www.leica-microsystems.com/products/microscope-software/details/product/leica-las-x-ls/
Olympus Fluoview FV10-ASW	Olympus	http://www.photonics.com/Product.aspx?PRID=47380
Olympus cellSens Software	Olympus	http://www.olympus-lifescience.com/en/software/cellsens/
Visual Studio Code 1.66.0	https://code.visualstudio.com/	N/A
Python 3.10.2	https://www.python.org/downloads/release/python-3102/	N/A
OpenCV 4.5.3	https://opencv.org/opencv-4-5-3/	N/A
Origin Pro 2020b	https://www.originlab.com/	N/A

RESOURCE AVAILABILITY

Lead contact

Further information and requests for resources and reagents should be directed to and will be fulfilled by the lead contact, Akira Satoh (satoha@cc.okayama-u.ac.jp).

Materials availability

Materials used in this study are available from the lead contact upon reasonable request.

Data and code availability

- Microscopy data reported in this paper will be shared by the lead contact upon request.
- Code used for analysis of the orientation of collagen fibers made in Python can be found in Table S1. All programs and packages used are publicly available and listed in the key resources table.
- Any additional information required to reanalyze the data reported in this paper is available from the lead contact upon request.
- All data are available in the main text or supplementary materials. Other data that support the findings of this study are available from the corresponding author, A.S., upon reasonable request.

EXPERIMENTAL MODEL AND SUBJECT DETAILS

Wildtype axolotls (*A. mexicanum*) and GFP transgenic axolotls were obtained through Hiroshima University Amphibian Research Funding and housed in aerated water at 22°C. For surgical experiments in this study, adult axolotls with nose-to-tail lengths of 10–16 cm were used and were not biased toward specific sex. Rat skin was a gift from Dr. S. Aizawa. The skin pieces were harvested from the lower limb of adult rats that had been cryopreserved after sacrifice. Rats used in this study were not biased toward specific sex. In this study, the care and treatment of animals were carried out under protocols approved by the Animal Care and Use Committee of Okayama University. All animal experiments were performed following the guidelines of the Animal Care and Use Committee of Okayama University. Every effort was made to minimize animal suffering in accordance with the NIH Guide for the Care and Use of Laboratory Animals.

METHOD DETAILS

Skin wounding and limb amputation

Axolotls were anesthetized in MS222 (Sigma, St. Louis, US) before surgery. As the skin injury, a 2-mm-square full-thickness excisional wound was made on the dorsal side of limbs (Figures 5, 7, S4 and S5). Limb amputations were performed on the upper limb (Figures 6, 7 and S5). As nerve deviation, nerve bundles were deflected to the wounded skin with a 2-mm-square full-thickness excision (Figure 7 and S5).

Histology

Harvested limbs were fixed in 4% paraformaldehyde at room temperature overnight. To prepare frozen sections, fixed samples were decalcified in 10% EDTA at room temperature overnight, equilibrated in 30% sucrose/PBS at room temperature overnight, and frozen in O.C.T. compound (Sakura Finetek). Frozen sections were cut to 12 μm thickness using a CM1850 cryostat (Leica) and dried. To prepare paraffin sections, fixed samples were decalcified in G-Chelate Quick (Geno Staff) at 4°C for 3 days, washed in distilled and deionized water (DDW), neutralized with G-Chelate-NT (Geno Staff) at 4°C overnight, equilibrated in 30% sucrose/PBS at room temperature overnight, dehydrated in ethanol and G-NOX (Geno Staff), and infiltrated with paraffin. Paraffin sections of 10 μm thickness were prepared using RX-860 (Yamato). Collagen fibers were visualized using a Picrosirius Red Stain Kit (Polysciences) according to the instruction manual. Images were acquired using a BX61 microscope (Olympus).

Plasmid transfection

For visualizing the fibers of type I collagen in dermal skin, we designed a GFP-Col1a2 plasmid vector containing a CMV promoter-secretory signal-$(Gly_4Ser)_3$ linker-AcGFP-$(Gly_4Ser)_3$ linker-Col1a2-SV40 poly A signal based on pCS2 plasmid (Figure S2). For visualization of cell morphology, we used a mCherry plasmid vector containing a CMV promoter-mCherry-SV40 poly A signal based on the pCS2 plasmid. Plasmid solution (0.4–2 μg/μL) was mixed with Fast green dye for visualization and injected under the skin of an axolotl limb using a fine glass capillary. Immediately after injection, electric pulses were applied (20 V, 50 ms pulse length, 950 ms interval, 10 times).

In vivo live imaging of collagen-producing process

GFP-Col1a2 and mCherry plasmid vectors were co-transfected into intact skin of axolotl limbs. The day after transfection, the *in vivo* GFP and mCherry signals were observed using an inverted two-photon

microscope TCS SP8 MP (Leica) with 63× magnification with a water immersion lens (Leica, HC PL APO 63×/1.20 W CORR CS2). Using InSight DeepSee femtosecond infra-red laser (Spectra-Physics), 900 nm was chosen as excitation wavelength, and GFP and mCherry signals were detected through filters of 500–550 nm and 580.5 to 653.5 nm, respectively. The z-step size was set to 1 μm. Amira software was used to align the images. To visualize the structure of an entire single cell, maximum intensity projection was applied to the confocal images using Fiji software. Adjustments of brightness and contrast were applied to figure images using Fiji software.

Immunofluorescence

In order to amplify the fluorescence of GFP in GFP-Col1a2 transfected skin, we performed whole-mount immunofluorescence for GFP. Skin pieces were harvested 5 days after transfection, then fixed in 4% paraformaldehyde at room temperature for 1 to 3 h, washed in TBST, then blocked for 1 h with 0.5% blocking buffer/PBS. Skin pieces were then incubated at 4°C overnight with primary antibody, anti-GFP pAb (1:500, MBL Cat# 598, RRID:AB_591819), in blocking buffer. The next day, skin pieces were washed in TBST, blocked for 1 h with 0.5% blocking buffer/PBS, and then incubated with secondary antibody, anti-rabbit IgG Alexa 488 (1:500, Thermo Fisher Cat# A32731, RRID:AB_2633280), at room temperature for 2 h, then incubated with 1.25 μg/mL Hoechst 33342 Solution (Nacalai, #19172-51) in TBST for 5 min, washed in TBST, and mounted in Fluoromount (DBS). The signals of Alexa Fluor 488 and mCherry (without immunofluorescence staining) in the skin were acquired using a confocal laser scanning microscope, FV1200 (Olympus), inverted type of TCS SP8 MP (Leica), FV300 (Olympus). To visualize the structure of an entire single cell, maximum intensity projection was applied to the confocal images using Fiji software. Adjustments of brightness and contrast were applied to figure images using Fiji software. Three-dimensional construction of collagen and fibroblast structure was performed using Amira software.

To investigate the relationship between cell morphology and *Col1* expression, immunofluorescence for mCherry was performed on skin sections. mCherry (E5D8F) Rabbit mAb (1:500; CST Cat# 43590, RRID:AB_2799246) was used as the primary antibody and anti-Rabbit IgG Alexa 594 (1:500, Thermo Fisher Cat# A-21207, RRID:AB_141637) was used as the second antibody. Images were acquired using a BX61 microscope (Olympus).

In situ hybridization

To investigate whether lattice-shaped cells express type I collagen, *in situ* hybridization for *Col1a1* and *Col1a2* was performed. Skin pieces were harvested five days after transfection of mCherry vectors, then fixed in 4% paraformaldehyde at 4°C overnight, and frozen in O.C.T. compound (Sakura Finetek). Frozen sections were cut at 20 μm thickness using a CM1850 cryostat (Leica) and dried. *In situ* hybridization was performed on each frozen section as previously described (Mitogawa et al., 2015). Digoxigenin (DIG) -labeled antisense RNA probes for axolotl *Col1a1* (AXOLOTL-OMICS, Am_2.2, AC_02200027944.1) and axolotl *Col1a2* (AXOLOTL-OMICS, Am_2.2, AC_02200044881.1) were used to perform *in situ* hybridization. To synthesize DIG-labeled RNA probes, reverse transcription was performed using SP6 or T7 RNA polymerase (TaKaRa) and DIG NTPs (Roche), and then the probes were hydrolyzed to short fragments. Sections were washed twice in PBST for 5 min each at room temperature, treated with 5 μg/mL proteinase K (Thermo Fisher) for 20 min, washed twice in PBST for 5 min each, post-fixed in 4% paraformaldehyde for 20 min, washed twice in PBST for 5 min each, and hybridized with DIG-labeled RNA probes (*Col1a1* or *Col1a2*) in the hybridization buffer (5× SSC (pH 5.0) containing 50% formamide, 50 μg/mL tRNA, 0.1% CHAPS, 100 μg/mL heparin, 1× Denhart, 10 mM EDTA, 0.1% Tween 20) at 62.5°C overnight. After hybridization, sections were washed twice in 5× SSC (pH 5.0) containing 50% formamide for 15 min each at 62.5°C, washed three times in 2× SSC (pH 5.0) containing 50% formamide for 15 min each at 62.5°C, washed in TBST at room temperature for 10 min, incubated in blocking buffer (0.5% blocking reagent [Roche] in TBST) at room temperature for 30 min, incubated with anti-DIG-AP, Fab fragments (1:1000; Roche Cat# 11093274910, RRID:AB_514497) at room temperature for 2 h, and washed four times in TBST 10 min each at room temperature. Sections were stained in NTMT (100 mM NaCl, 100 mM Tris-HCl [pH 9.5], 0.1% Tween 20) containing 37.5 μg/mL 5-bromo-4-chloro-3-indolyl phosphate and 37.5 μg/mL nitro blue tetrazolium chloride in the dark at room temperature for 2 h. The coloring reaction was stopped in TE buffer. After *in situ* hybridization, immunofluorescence was performed to detect mCherry signals. Images were acquired using a BX61 microscope (Olympus).

SEM and SHG imaging

SEM imaging was performed by Hanaichi Ultrastructure Research Institute, Co., Ltd. Collagen structure was detected by SHG imaging using an inverted two-photon microscope TCS SP8 MP (Leica) with 63× magnification with a water immersion lens (Leica, HC PL APO 63×/1,20 W CORR CS2). Fixed skin was mounted in Fluoromount and photographed under the microscope from the dermal side. Using InSight DeepSee femtosecond infra-red laser (Spectra-Physics), 900 nm was chosen as excitation wavelength, and SHG signals and GFP signals amplified with Alexa Fluor 488 were detected through filters of 435–485 nm and 500 to 550 nm, respectively. The z-step size was set to 0.8 μm.

Decellularization of the dermis and cell culture

Decellularization and ECM preparation were performed as follows. Axolotl skin was removed from the limb and the epidermis was scraped and removed by forceps. Then, the skin (dermis) was washed several times in DDW. The washed dermis was then placed in a 2 M urea solution for 1 week. The 2 M urea solution was changed on day 1 and 3. Then, the sample was washed in DDW 5 times. For imaging, the samples were mounted by Softmount. For cell culture, the decellularized dermis was flattened and dried. Next, the flattened dermis was pinned on a non-coated regular plastic dish using waterproof glue. The dish was washed with culture medium 3 times and used. Dermal fibroblasts were obtained from GFP animals. The limb skin was removed from a limb. The removed skin was dissected into pieces, and then incubated in the collagenase solution (0.5% collagenase (Wako, #032–22364)/70%PBS/DDW) at room temperature for 4 h. An equal volume of trypsin solution (0.5%Trypsin/0.05%EDTA/PBS) was added into the collagenase solution and incubate for 30 min. The cell suspension was filtered through a 40 μm cell strainer (Falcon, #352340). The enzymatic digestion was neutralized by adding an equal amount of the culture medium (50%Glutamax DMEM/10% FBS/40% DDW/0.01M HEPES [pH. 7.5], 0.3 mg/mL Gentamycin). Cells were washed with medium a couple of times and cultured on a plastic dish (Falcon, #3001) for a day in order to remove keratinocytes. Then the attached cells on the plastic dish were collected and replated on the decellularized dermis. 5 days after the plating, the cells were fixed with 4% paraformaldehyde at room temperature for 10 min, then immunostained with anti-GFP pAb antibody. Cell nuclei were stained with Hoechst33342.The pictures were captured using a BX61 light microscope (Olympus).

QUANTIFICATION AND STATISTICAL ANALYSIS

Analysis for the orientation of collagen fibers

We collected 40–90 SHG images in digital for every 0.8 μm depth of the dermal layer. For the orientation analysis, an area in the range of 512 × 512 pixels, corresponding to 92.26 × 92.26 μm, was extracted from a digital SHG image with 8-bit depth. The image of the extracted area was processed with Gaussian filter whose kernel of 2 pixels to reduced salt-and-pepper noise and with Sobel filter to enhance the edges. The processed image was transformed a function of position [pixels] to a function of frequency [cycles/pixel] with a discrete fast Fourier transform (DFFT) alogism. Here, we set up a fan-shaped region of interest (ROI) in a frequency-angle (r-θ) coordinate after the DFFT process, with a range of 25–65 [cycle/pixel] in r and $\pm$ π/60 [rad] in θ. The ROI was scanned every π/30 [rad] from 0 to π and from π to 2π, and the mean power in each ROI was calculated. The two of obtained plots of degree vs mean power were merged in to a graph. The data for θ = 0, π/2, π, 3π/3, and 2π was not included to remove the analytical artifact by discrete calculation. Thus, we obtained angle dependence of DFFT power. We calculated the angle dependence of five images near the just focus depth and averaged them to a single graph. Data in Figures 7J–7M and S5 were presented as mean $\pm$ standard deviation (SD). The image processing procedure was performed using a homemade software programmed by Python (ver. 3.10.2) and OpenCV library (ver. 4.5.3). Code used for analysis is shown in Table S1.

Assuming the two independent normal distributions in the graph, we fitted the graph as a function of angle θ with double Gaussian function as following,

$$f(\theta) = a_1 \exp\left\{ -\frac{(\theta - \theta_1)^2}{2{\sigma_1}^2} \right\} + a_2 \exp\left\{ -\frac{(\theta - \theta_2)^2}{2{\sigma_2}^2} \right\} + C,$$

where a_1 and a_2 are proportional constant, θ_1 and θ_2 are centers of Gauss distribution, ${\sigma_1}^2$ and ${\sigma_2}^2$ are variances of Gauss distribution, and C is offset. The fitting process was performed using Origin Pro 2020b (Lightstone Corp, Tokyo).